Supplementary Information (SI)

Size-dependent bending of a rectangular polymer film

Yin Liu[1,#], Xuemei Fu[2,#], Ruochen Yang[2,#], Jun Liu[1],
Benjamin Chee Keong Tee[2-3], Zhuangjian Liu[1,*]

[1]Institute of High Performance Computing (IHPC), Agency for Science, Technology and Research (A*STAR), 1 Fusionopolis Way, Singapore, 138632 Republic of Singapore
[2]Department of Materials Science and Engineering, National University of Singapore, Singapore 117575, Singapore.
[3]Institute for Health Innovation and Technology, National University of Singapore, Singapore 117599, Singapore.

[#] These authors contribute equally to this work.
[*]Corresponding Author: liuzj@ihpc.a-star.edu.sg

S1 The finite element model

We use commercial finite element package, Abaqus, to simulate the coupled finite deformation and acetone diffusion. For convenience, the balance equations for the coupled problem are again shown as following

$$Balance\ of\ momentum\text{:}\quad \nabla \cdot P + b = 0 \tag{S1}$$

and

$$Balance\ of\ fluid\ diffusion\text{:}\quad \frac{\partial C}{\partial t} = D\left(\frac{\partial^2 C}{\partial x^2} + \frac{\partial^2 C}{\partial y^2} + \frac{\partial^2 C}{\partial z^2}\right) \tag{S2}$$

The variables in Eqs. (S1) and (S2) are the same as those in the main contexts.

Since the module for direct dealing with Eq. (S1) seems not available in Abaqus, and we make an analog between the governing equations for fluid diffusion and heat transfer, so that we can

utilize the structural-thermal coupling module to simulate this problem. The balance equation for transient heat transfer is given by

$$\frac{\partial T}{\partial t}=\frac{k}{\rho c_{\rho}}\left(\frac{\partial^2 T}{\partial x^2}+\frac{\partial^2 T}{\partial y^2}+\frac{\partial^2 T}{\partial z^2}\right) \tag{S3}$$

where T is the temperature, k is the coefficient of heat conduction and c_{ρ} is the heat capacity. Comparing Eqs. (S2) and (S3), we obtain analogous relations

$$C\sim\alpha T \text{ and } D\sim\frac{k}{\rho c_{\rho}} \tag{S4}$$

where α is the coefficient of thermal expansion. In the simulation, we assume that $T=0$ (or $C=0$) represents the initial non-swelling state and $T=1$ (or $C=\alpha$) the final fully swelling state. As stated earlier, the acetone diffusion in the polymer network causes swelling of the bulk material, which is equivalent to applying volumetric expansion strain ε^{v} to the material. Thus, we may obtain the relation,

$$\varepsilon^{v}\sim\alpha\Delta T\sim\Delta C \tag{S5}$$

where ΔT is the temperature change. In this way, we realize the coupling between the finite deformation and the fluid diffusion.

We use an incompressible Mooney-Rivlin model to characterize the elastic deformation of the material, where the strain energy function is given by

$$W=C_{10}(I_1-3)+C_{01}(I_2-3)+p(J-1) \tag{S6}$$

where $I_1=trC$, $I_2=\frac{1}{2}[(trC)^2-tr(C\cdot C)]$, $J=\det F$, $C=F^TF$ is the right Cauchy-Green tensor, F is the deformation gradient, p is a Lagrange multiplier enforcing the incompressibility condition, i.e., $J=1$, and C_{10} and C_{01} are constant constitutive parameters. We will introduce the calibration of the material parameters in the next section. The boundary conditions of the finite element model are detailed in Figure S1. The element type used for simulation is C3D8R and the finite element mesh is fine enough to obtain converged results.

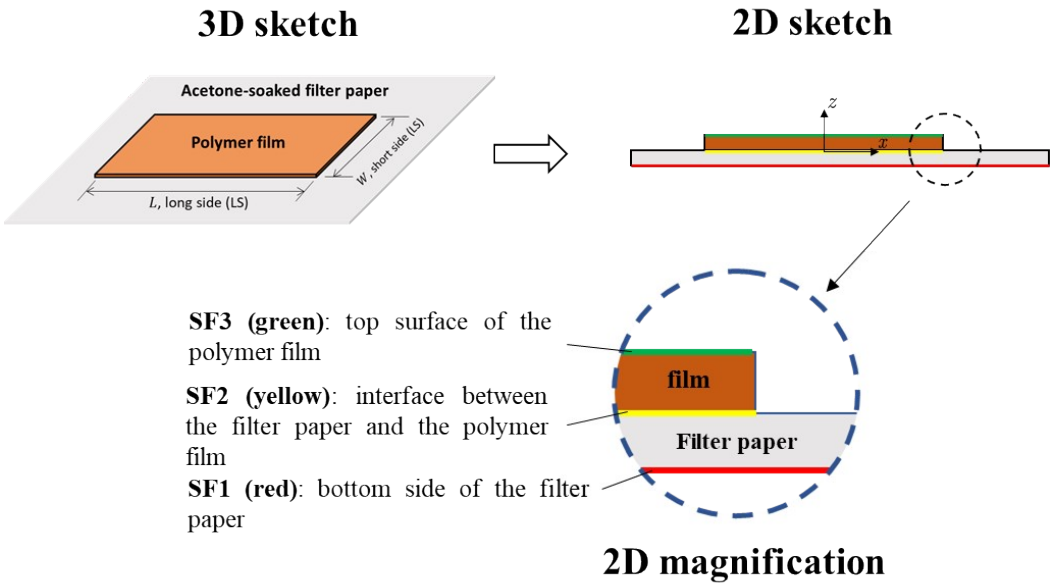

Figure S1 The sketch for the fluoroelastomer film placed on an acetone-soaked filter paper. The location of three interfaces S1, S2 and S3 are highlighted, which are essential to capture the coupled large deformation and diffusion process. The rigid displacements of the film are constrained by fixing symmetric degrees of freedom (DOFs) at the symmetric axis of the film. At SF1, all the displacement degrees of freedom (DOFs) are fixed to be zero. At SF2, a convective boundary condition (Thermal conductance interaction in Abaqus) is applied for acetone diffusion from the filter paper to the film, which satisfies $q(t) = h(d)(T(0,t) - T_0)$, where $T_0 = 1$ denotes the acetone concentration in the filter paper, $h(d) = \begin{cases} h_0(d_0 - d), for\ d < d_0 \\ 0, \qquad\quad for\ d \geq d_0 \end{cases}$ and with $h_0 = 0.8 \times 10^{-3}$ and $d_0 = 2\ mm$ (see more details in Section S2). Mechancial surface to surface contact is applied at SF2. At SF3, a convective conduction (Surface film condition in Abaqus) is applied, despite its negligible effect, to describe the acetone evaparation from the film to external environment, which is given by $q(t) = h_e(T(H,t) - T_e)$ with $T_e = 0$ and $h_e = 1 \times 10^{-7}$.

S2 Identification of the material parameters

We conduct uniaxial tension experiment of rectangle strips to determine the material parameters C_{10} and C_{01} in Eq. (S6). In the case for uniaxial tension, the deformation gradient is given by $F = diag\left(\lambda, \frac{1}{\sqrt{\lambda}}, \frac{1}{\sqrt{\lambda}}\right)$, and thus $I_1 = \lambda^2 + \frac{2}{\lambda}$ and $I_2 = \frac{1}{\lambda^2} + 2\lambda$. The corresponding tensional (nominal) stress is given by

$$P_{11} = 2C_{10}\left(\lambda - \frac{1}{\lambda^2}\right) + 2C_{01}\left(1 - \frac{1}{\lambda^3}\right) \tag{S7}$$

The parameters, C_{10} and C_{01}, are obtained by numerical fitting between the expression in Eq. (S7) and the experimental stress-stretch data (Figure S2). Three groups of data for rectangle samples with the same dimensions are used. We find that the results for the constitutive equation (S7) with $C_{10} = 0.005$ and $C_{01} = 0.17$ agree well with experimental results (Figure S2). The Young's modulus at the ground state is given by $E = \left.\frac{\partial P_{11}}{\partial \lambda}\right|_{\lambda=1} = 6(C_{10} + C_{01}) = 1.05\ MPa$.

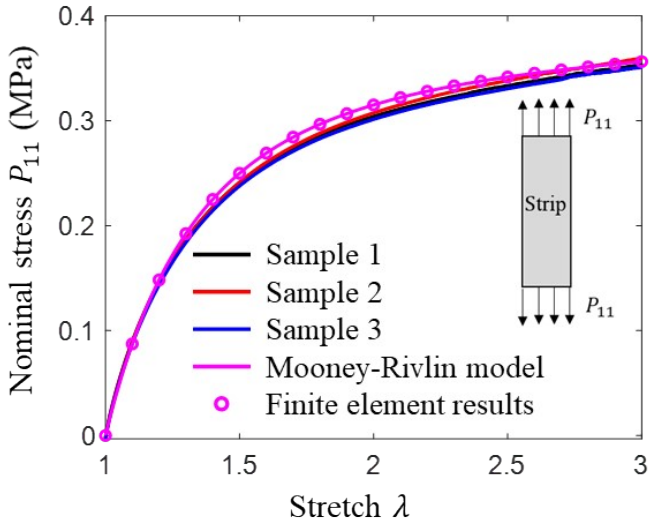

Figure S2 Comparison of the stress-stretch relations between experiment, theory and finite element model. The experiment data were obtained by stretching three strip samples with the size of $L \times W \times H \sim 80\ mm \times 5\ mm \times 1.4\ mm$, where L, W and H are the length, width and thickness of the strip.

To identify the diffusion coefficient $D \sim \frac{k}{\rho c_\rho}$, we first set $\rho c_\rho = 1$, which does not change the essential properties of solution and thus problem comes down to identifying k. We introduce a simplified one-dimensional diffusion problem in the thickness direction (z-direction, Figure S3), based on Eq. (S2) and $D \sim \frac{k}{\rho c_\rho} \sim k$ ($\rho c_\rho = 1$),

$$\frac{\partial T(z,t)}{\partial t} = k\frac{\partial^2 T(z,t)}{\partial z^2} \tag{S8}$$

with the boundary condition $q(t) = h_0(T(0,t) - T_0)$ at the bottom side (Figure S3), and initial condition $T(z,0) = 0$, where h_0 is a conduction coefficient measuring the intensity of heat conduction (fluid permeation) when the filter paper and the film contact perfectly, and $T_0 = 1$ representing the fully swollen state. As $t \to \infty$, we expect that $T(0,\infty) \to T_0 = 1$ and $q(\infty) = 0$.

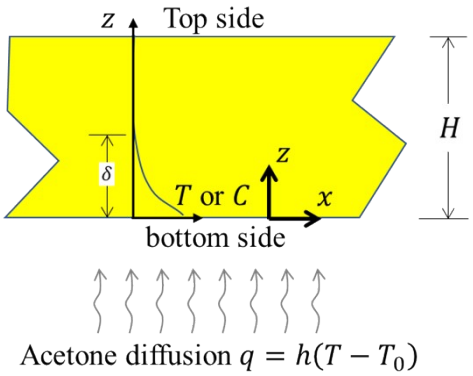

Figure S3 Sketch of the one-dimensional fluid diffusion (heat conduction) across the thickness direction of the film.

The solution to Eq. (S8) is given by

$$T = erfc\,\zeta - \exp\left[\beta(2\zeta + \beta)\right] erfc\,(\zeta + \beta) \tag{S9}$$

where $\zeta = \frac{y}{2\sqrt{\alpha t}}$, $\beta = h\sqrt{\alpha t}/k$, $\alpha = k$, $erfc\,x = 1 - erf\,x$ and $erf\,x = \frac{2}{\sqrt{\pi}} \int_0^x e^{-\theta^2} d\theta$. By setting specific value for the material parameters k and h, we can obtain distribution of T as a function of z and t (or C, see Figure S4a for the case $k = 1.5 \times 10^{-4}$ and $h_0 = 0.8 \times 10^{-3}$), from which we can extract the distance of the diffusion front to the bottom side, i.e., δ in Figure S3. The value of δ can be readily measured by observing the diffusion process of acetone inside a film and thus can be used to fit the parameters k and h_0 (Figure S4b). We find that the parameters $k = 1.6 \times 10^{-4}$ and $h_0 = 0.8 \times 10^{-3}$ fits the experiment data very well and the diffusion velocity increases with the diffusion coefficient k as expected (Figure S4b). The expansion coefficient α is determined by the maximum swelling ratio of fluoroelastomer, which is $\alpha T^{max} = \alpha = 1.02$ (due to $T^{max} = T_0 = 1$). All the material parameters are summarized in Table 1.

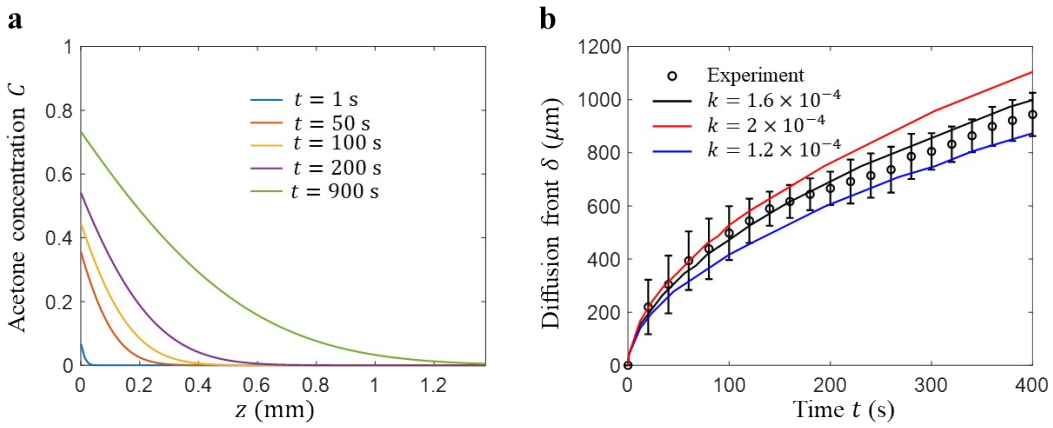

Figure S4 (a) Variation of C or T as a function of location and time for $k = 1.5 \times 10^{-4}$ and $h = 0.8 \times 10^{-3}$. (b) Comparison between the analytical expression with varying k and $h = 0.8 \times 10^{-3}$ and experimental data.

Table 1 The constitutive parameters used for finite element simulation of transient swelling of the fluoroelastomer film.

Parameters	C_{10} (MPa)	C_{01} (MPa)	ρ (Kg/m³)	$c_\rho = 1/\rho$	$k\ (J \cdot m/K)$	α	$h_0\ (J/K)$
Values	0.005	0.17	1.8×10^3	0.556×10^{-3}	1.6×10^{-4}	1.02	0.8×10^{-3}

S3 Supplementary results

To validate the analytical curvature expression in Eq. (15), For this purpose, we consider a bilayer with the following parameters $L = 20\ mm$, $W = 10\ mm$, $H = 2H_a = 2H_p = 0.2\ mm$, $\rho_a = \rho_p = 1.8 \times 10^3\ Kg/m^3$, $E_a = E_p = 1.0 \times 10^6\ Pa$, $\nu = 0.3$. Consequently, Equation (15) simplifies to

$$\kappa H = 1.95\alpha - 0.004 \tag{S10}$$

If no gravity is counted and the bilayer bends along the long side, the curvature becomes $\kappa H = 1.95\alpha$, which exhibits good agree with the numerical results (Figure S5a). However, when the gravity effect is taken into account with the bilayer bending along the short side, the numerical results is slightly lower than the expression in Eq. (S10) (Figure S5b). This disparity arises from our assumption that the bilayer bends into a cylindrical shape, which is not the case when the bilayer is in the initial state under gravity. To rectify this, we introduce the deflection w based on the beam theory in small deformation. (for short-side bending along the y direction, Fig. 2)

$$w = -\frac{\rho g H y^2}{24EI}\left(\frac{3}{2}W^2 - 2Wy + y^2\right), y \in [0, W/2] \tag{S11}$$

where $I = H^3/12$. It can be obtained that the curvature of the curve w at $y = 0$ is given by $(\kappa H)_{beam} = w''(y = 0) = -0.0132$. If the modified value -0.0132 is used in Eq. (S10), the analytical results show better agreement with the numerical results (Figure S5b). For sake of theoretical solution (e.g., derivation of Eq. (19)), we use the curvature expressions in Eqs. (11) and (15), which maintains the intrinsic deformation features of the bilayer. The curvature is calculated by the least square method using the coordinates of twelve points (marked in Figure S5c) near the origin (0,0,0).

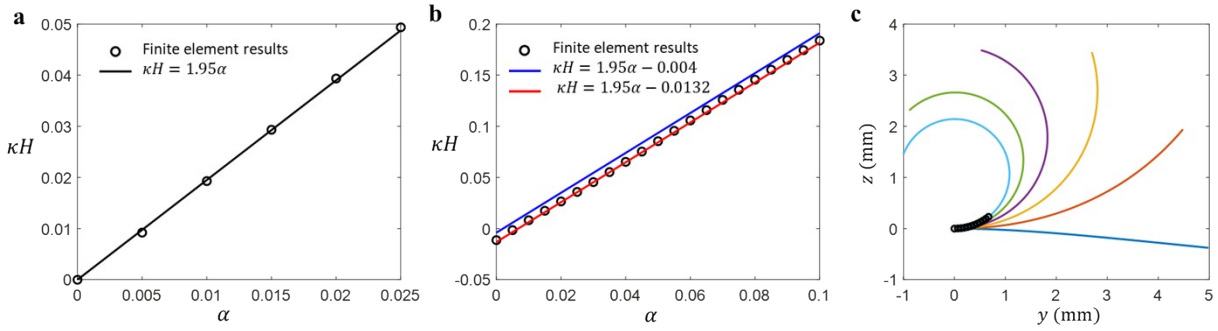

Figure S5 Validation of the analytical results obtained by the bilayer model. (a) Comparison of the curvature without the gravity effect. (b) Comparison of the curvature with the gravity effect. (c) Deformed shape of the line in the bending direction for α = 0, 0.02, 0.04, 0.06, 0.08 and 0.1.

Using the finite element mode and calibrated parameters, we simulate the bending process of the film for multiple groups of geometrical parameters L, W and H. Figure S6a and b show temporal variation of the distance between the middle points at the opposite sides for samples with $H = 900\ \mu m$ and $1255\ \mu m$, respectively. The simulation results agree well with the measured data and the bending configurations (Figure S6), which indicates the accuracy of the finite element model.

Figure S7 shows the simulation results for the bilayers and the fluoroelastomer film with and without applying the gravity in the finite element model. The gravity shows profound influence on the bending direction of the film. In both cases, the structure bends along the long side without gravity and along the short side with gravity. The fluoroelastomer film shows large swelling degree (as well as the bending curvature) in the middle region with continuous contact with the acetone-soaked filter

paper during deformation (Figure S7b), while the bilayer deforms into a cylinder (Figure S7a) with nearly uniform curvature due to uniform swelling strain applied at the bottom layer.

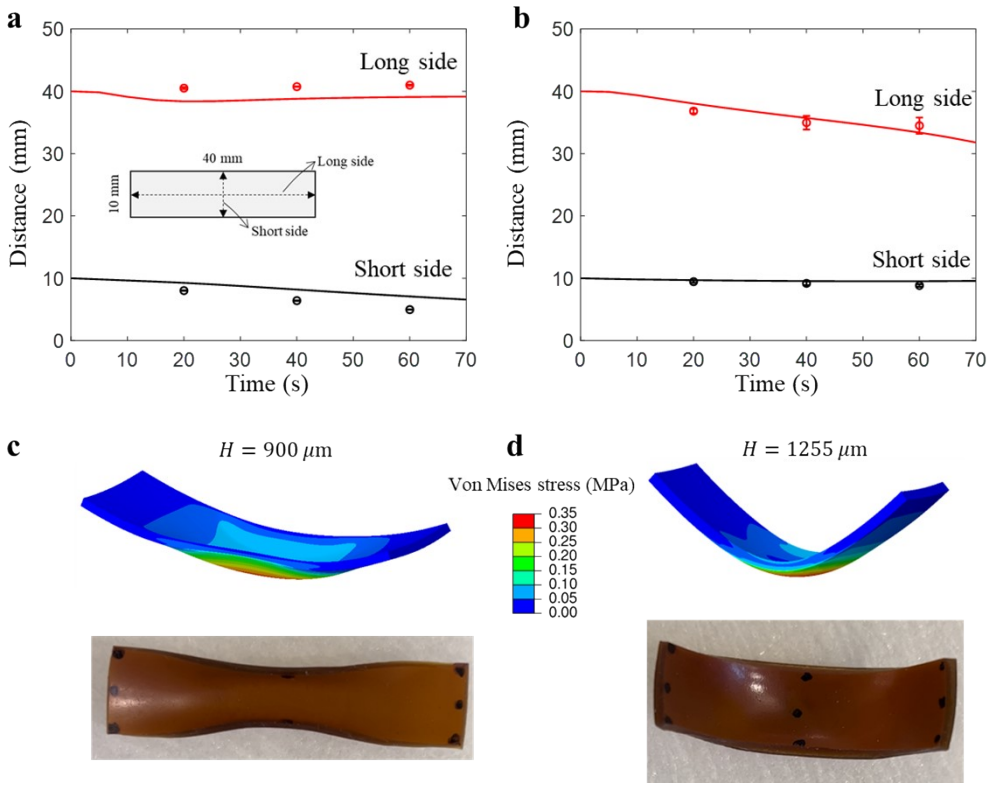

Figure S6 Temporal variation of middle point distance along the short and long sides of rectangle films for different thicknesses (a) $H = 900\ \mu m$ and (b) $H = 1255\ \mu m$. The size of the film is 40 mm × 10 mm. (c) and (d) Comparison of the bending configuration at 1 min between the finite element and experimental results. The contour shows the distribution of the Von Mises stress.

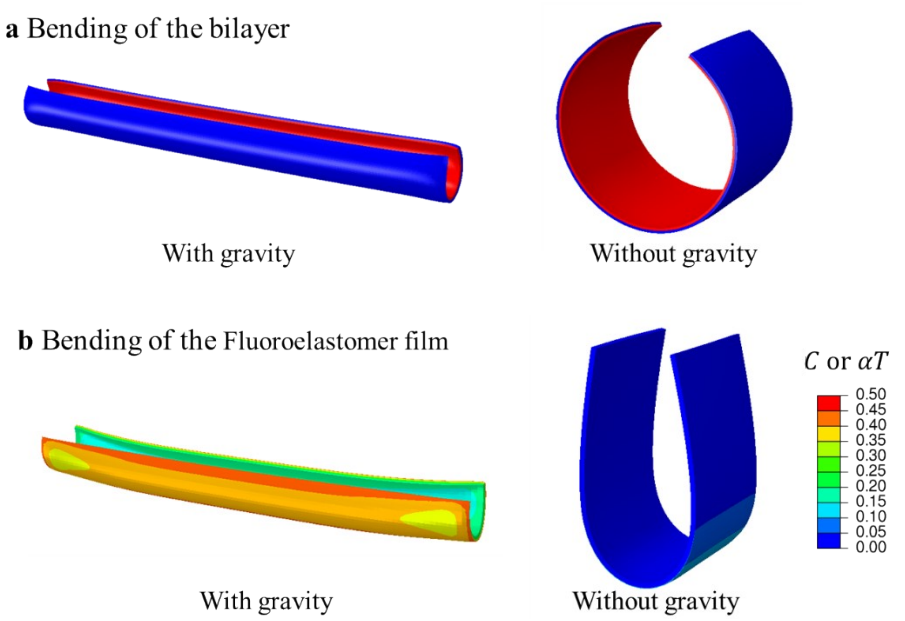

Figure S7 (a) Bending modes of a bilayer with and without the gravity effect. The model assumptions and the finite element settings are addressed in Section 2 of the main text. The top and bottom layer are colored by red and blue, respectively. (b) Bending modes of the fluoroelastomer film with and without the gravity effect. The contour denotes the acetone concentration or swelling strain. The sizes for all the cases are $L \times W \times H = 20 \times 5 \times 0.2\ mm^3$.

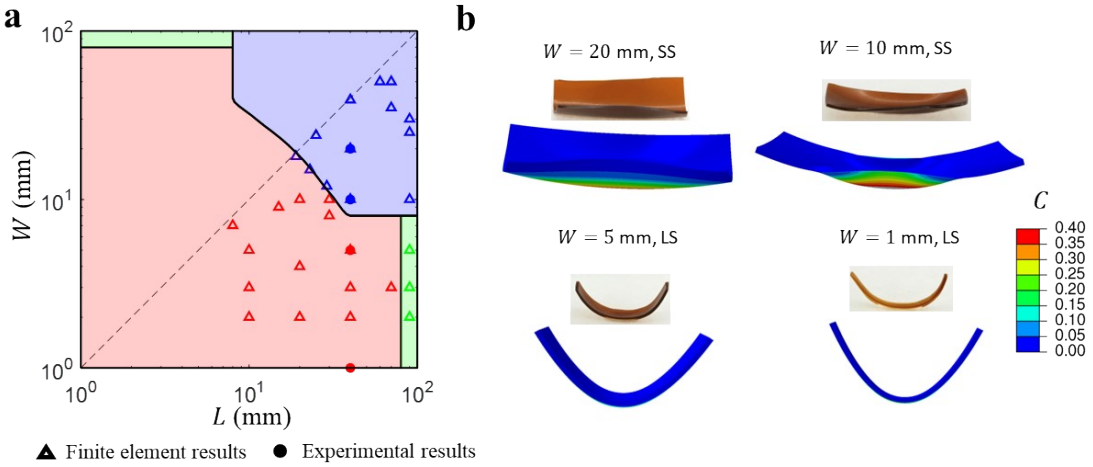

Figure S8 (a) Phase diagram for size-depndent bending modes for $H = 900\ \mu m$. (b) Some representative configurations with varying $W = 20$, 10, 5, 1 mm and $L = 40\ mm$, $H = 900\ \mu m$.

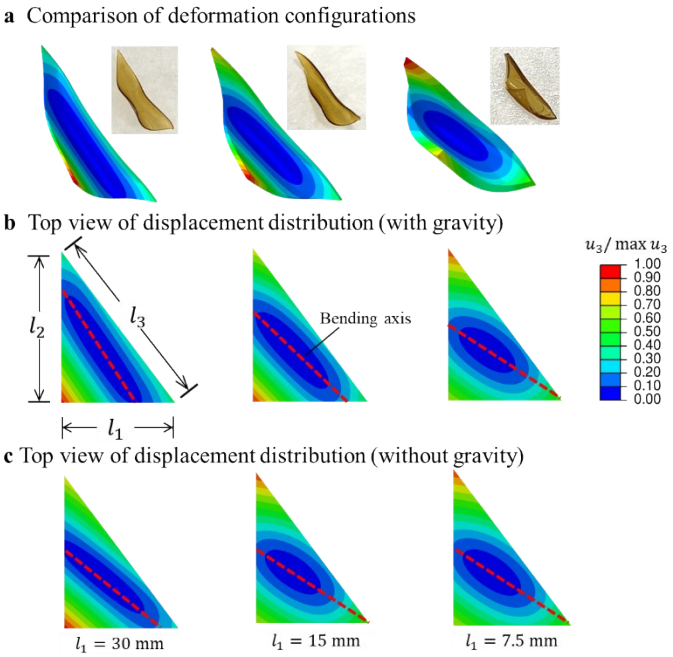

Figure S9 Size-dependent bending of triangular films, which are of a fixed edge ratio l_1:l_2:l_3 = 3:4:5 and varying overall sizes $l_1 = 30$, 15 and 7.5 mm from the left to the right. (a) Comparison of deformation between experiment and simulation, where the contour represents normalized deflection (displacement perpendicular to the film), $u_3/\max(u_3)$. (b) and (c) top view of the displacement distribution in the undeformed configuration with and without gravity effect. The bending axes are determined by the location of minimum displacement and marked by red dash line. For small-sized films (e.g., $l_1 = 7.5$ mm), the bending axis is not affected by gravity, while for large-sized film ($l_1 = 30$ mm), we observe obvious rotation of the bending axis.